PAPER

Check for updates

pH-Triggered nanostructural transformations in antimicrobial peptide/oleic acid self-assemblies†

Mark Gontsarik, [a,b] Mahsa Mohammadtaheri, [a] Anan Yaghmur [b] and Stefan Salentinig *[a]

The delivery of poorly water-soluble antimicrobial peptides (AMPs) that are sensitive to degradation is a major challenge in the pharmaceutical field. In this study, we design and characterize a pH-sensitive nanocarrier with the potential for delivery of AMPs and their protection from degradation. These nano-biointerfaces are prepared through the self-assembly of oleic acid (OA) with the human cathelicidin LL-37 in excess water. Advanced experimental methods including synchrotron small angle X-ray scattering, cryogenic transmission electron microscopy, and dynamic light scattering were used to characterize the OA/LL-37 self-assemblies and their structural alterations in response to changes in pH and composition. Experimental findings reveal colloidal transformations from normal emulsions *via* micellar cubosomes and hexosomes to vesicles upon increasing the pH from 6.0 to 8.0 at a LL-37 content around 10 wt% relative to OA. Increasing the LL-37 content to 30 wt% in OA led to diminishing of micellar cubosomes and hexosomes in this narrow pH range, favoring the formation of micelles and vesicles of various shapes and sizes. Upon increasing the pH, with the strongest effect around pH 7.5, charge repulsions among the gradually deprotonating carboxylic groups of OA modified the geometric packing of the molecules, significantly affecting the nanostructure. These detailed insights into the formation of this unique family of nanobiointerfaces and their tunable structural features may contribute to the rational design of pH-responsive antimicrobial systems for the delivery of peptides, particularly poorly water-soluble AMPs.

Introduction

Stimuli-responsive nanocarriers, based on inverse non-lamellar lyotropic liquid crystalline (LLC) structures and microemulsions, have been of recent interest for functional food and drug delivery applications, owing to their unique structural features. They are attractive for targeted delivery of hydrophilic, amphiphilic, and hydrophobic bioactive components.[1,2] By exploiting the dynamic nature of these LLC structures, different types of responsive self-assemblies have been designed that are sensitive to stimuli such as specific enzyme activation,[3–5] light,[6–8] and pH.[1,2,9–11] In the design of nanocarriers for poorly water-soluble antimicrobial peptides (AMPs), there is particular interest in the development of pH-responsive systems owing to their self-regulated passive targeting and fairly broad range of biomedical and pharma-

ceutical applications.[12] In this context, AMPs are gaining increasing attention as promising alternatives to conventional antibiotics in the light of the global emergence of antibiotic resistance.[13] The commonly shared features among more than 2700 AMPs derived from natural sources so far are their relatively short amino acid sequence (average of 30 amino acids), their amphiphilicity with more than 30% hydrophobic amino acids, and their net positive charge at physiological pH.[14] Among these AMPs, there is particular interest in the use of LL-37, which plays a crucial role in the human innate immune system.[15,16] Owing to its amphiphilic nature, the human cathelicidin LL-37 targets the bacterial membrane, presumably inducing its destabilization through integration driven by strong intermolecular interactions with the membrane lipids.[17,18] However, AMPs such as LL-37 have poor water solubility, are unstable in biological systems due to chemical degradation,[19] and are even cytotoxic at high concentrations due to their non-specific mechanism of action.[18]

In these nanocarriers, the self-assembled inverse LLC or microemulsions form the internal oil-continuous structure of the emulsion droplet. This internal structure arises from the self-assembly of specific biologically relevant surfactant-like lipids in excess water.[20–25] Guest molecules, such as LL-37, can be encapsulated in these structures, and protected from the

aLaboratory for Biointerfaces, Department Materials meet Life, Empa Swiss Federal Laboratories for Materials Science and Technology, Lerchenfeldstrasse 5, 9014 St Gallen, Switzerland. E-mail: stefan.salentinig@empa.ch, stefan.salentinig@gmail.com
bDepartment of Pharmacy, Faculty of Health and Medical Sciences, University of Copenhagen, Universitetsparken 2, DK-2100 Copenhagen Ø, Denmark
†Electronic supplementary information (ESI) available. See DOI: 10.1039/c7bm00929a

surrounding aqueous environment by partitioning into the hydrophobic or the hydrophilic domains of these self-assemblies, or by localization at their water–lipid interfaces.[26–28] The release rate of encapsulated molecules to the surrounding medium was reported to depend on the internal structure of the nanocarrier.[29]

Our research group has recently demonstrated the spontaneous transfer of LL-37 from the surrounding excess water into the internal bicontinuous cubic $Im3m$ phase of glycerol monooleate (GMO) cubosomes.[30] This allows the preparation of such colloidal nanosystems, without the need for exposing the degradation-sensitive peptide to a high-energy input, such as ultrasonication, that may be necessary for dispersing the inverse hexagonal (H$_2$) phase, the inverse bicontinuous cubic phases ($Pn3m$ and $Im3m$ phases), and the inverse discontinuous (micellar) cubic $Fd3m$ phase into the so-called hexosomes, cubosomes, and micellar cubosomes, respectively. Intriguingly, the integration of LL-37 into the cubic LLC structure induced significant structural alterations and the antimicrobial activity of LL-37 in these tunable colloidal GMO-peptide self-assemblies correlated strongly with the structure type: the LL-37-loaded cubosomes (dispersion of the bicontinuous cubic $Im3m$ phase) were rather inactive, contrary to small vesicles and micelles that exhibited higher activity than the control sample (an aqueous solution of the free peptide).[30] The encapsulation of LL-37 into cubosomes and hexosomes based on GMO/oleic acid (OA) mixtures and their protection from enzymatic degradation in these structures were also reported.[27,31] However, to the best of our knowledge, the design of pH-responsive AMP nanocarriers based on specific lipids and their detailed nanostructural morphologies depending on the composition and pH have not yet been reported in the literature.

In this study, we report a simple structurally tunable and versatile pH-responsive system composed of LL-37 and OA and discuss the influence of pH and composition on the self-assembled nanostructure of these emulsions upon loading with LL-37. This understanding may be valuable for unraveling the intermolecular interactions between the AMP and the lipids that play an important role in the destruction of bacterial membranes. It may further contribute to the design of pH-triggered drug nanocarriers with particular potential for self-regulated passive targeting of AMPs. In pH-tunable nanosystems, the protonation and deprotonation of specific surfactants, such as long-chain fatty acids embedded in the self-assembled structure, modify the geometric packing of the molecules, leading to a change in the nanostructure.[1,11,32–37] Such pH-responsive nanostructures are typically detected during the digestion of model triolein emulsions[38] and food systems such as milk[39,40] and mayonnaise,[41] where these colloidal nanoobjects may sustain the release of poorly water-soluble food components and secure essential nutrient uptake of the body under compromised bile salt conditions.

OA has been selected for this study as it is an essential compound in many dietary oils and changing the pH of a normal OA emulsion has been previously reported to result in substantial changes in the self-assembly of the interior of the emulsion droplet.[11,35] At pH < 6.5, normal (OA-in-water) emulsions were obtained. Emulsions with an internal inverse micellar cubic $Fd3m$ phase (micellar cubosomes) were reported at pH ~ 7.0, with an internal inverse hexagonal H$_2$ phase (hexosomes) at pH ~ 7.5 and vesicles and normal micelles (L$_1$ phase) at pH > 8.[11,36,42–44] Intriguingly, the apparent pK_a value of OA in these self-assemblies was reported to be between 6.4 and 8.5, depending on the composition of the internal phase of the dispersed nanoobjects.[11,35] The major structural modifications due to a subtle variation in pH close to this apparent pK_a were observed.[11] The structural sensitivity of OA and OA/LL-37 dispersions to pH could be relevant in the development of nanosystems for different medical applications. For instance, the microenvironments of infected gum tissues and chronic wounds exhibit pH conditions of around 8.5 (ref. 45–47) and 8.0 (ref. 48 and 49) respectively. Hence, the elevated pH in infected locations could trigger structural transformations in such nanosystems, leading to activation of the antimicrobial activity.[30] In principle, this would also allow directing the antimicrobial activity to the affected tissues, while minimizing toxicity in other locations as LL-37 has been described to be antimicrobially active in the 0.02–16 μM range and cytotoxic at 13–25 μM.[15]

Following the LL-37-induced and pH-triggered structural alterations and phase changes in the OA/LL-37 self-assemblies by synchrotron small angle X-ray scattering (SAXS), cryogenic transmission electron microscopy (cryo-TEM), and dynamic light scattering (DLS), this study confirmed the integration of LL-37 into the interior nanostructure of OA nanoparticles at different pH values. The experimental findings revealed the formation of a pool of colloidal structures ranging from nanoparticles with highly ordered internal non-lamellar liquid crystalline phases to vesicles and micelles depending on the pH and composition.

Experimental section

Sample preparation

For the preparation of oleic acid (OA) emulsion, OA (≥99% purity, Sigma-Aldrich, Buchs, Switzerland) was mixed with 0.02 M phosphate buffer saline (PBS at pH 7.4 with 0.125 M NaCl and 0.0027 M KCl) that contained 0.2 wt% Pluronic F127 (BASF, Ludwigshafen, Germany) at a final OA concentration of 20 mg ml^{-1}. This crude oil-in-water emulsion was then homogenized by ultrasonication with a tip sonicator (Sonics Vibra Cell VCX 130 W, 20 kHz, Sonics & Materials Inc., Newton, CT, USA) in 3 successive cycles: 1 min in pulse mode (1 s pulse, 1 s break), 2 min in pulse mode (3 s pulse, 5 s break), and 2 min in pulse mode (3 s pulse, 5 s break) at 20%, 25%, and 27% of maximum amplitude, respectively. This process consistently led to colloidally stable dispersions. For the preparation of the OA/LL-37 nanocarriers, LL-37 in the form of trifluoroacetate salt (98.3% purity, Bachem AG, Bubendorf, Switzerland) was first dissolved in PBS at pH 7.4 and then mixed with the

already prepared OA emulsion at various weight ratios between 5 wt% and 30 wt% of LL-37 relative to OA. The total dispersed phase concentration (OA + LL-37) was kept constant at 20 mg ml^{-1}. The pH of the samples was adjusted using 1 M NaOH or 1 M HCl, and the samples were equilibrated for a minimum of 30 min prior to experiments. Ultra-pure water (resistivity >18 MΩ cm) was used for the preparation of all samples.

Cryogenic transmission electron microscopy (cryo-TEM)

Briefly, a 3 μl drop of the sample was placed on a Lacey Formvar holey film with a lacey structure enforced by a silicon monoxide coating, supported by a TEM copper grid (300 mesh, copper, purchased from Ted Pella Inc., Redding, CA, USA) and was then rapidly plunged into liquid ethane that was previously cooled close to its freezing point of −183 °C with liquid nitrogen. The vitrified specimen was stored under liquid nitrogen until analysis with a Zeiss 902A microscope (Jena, Germany) operating in zero-loss bright field mode at 80 kV with an underfocus of 1 μm. The images were digitally collected under low-dose conditions and the temperature was kept at −175 °C. A more detailed experimental procedure was previously described.[30]

Dynamic light scattering (DLS) and ζ-potential measurements

Characterization of the mean hydrodynamic radius (R_H), polydispersity index (PDI), and ζ-potential was carried out on a Malvern Zetasizer Nano ZS90 (Malvern Instruments, USA) with a He–Ne Laser beam at a wavelength of 633 nm. The measurements were performed at a scattering angle of 90° and with a laser power of 4 mW. The temperature was kept at 25 °C in all measurements. The R_H and the PDI of the particles were determined with the cumulant method (see the ESI† for more details).

Samples were diluted 1/100 with PBS at an appropriate pH and centrifuged for 10 min at 3000g prior to the measurements to remove any dust and debris. For R_H determination in the samples at pH 8.5, 1/10 dilution was used due to low scattering intensity. Both particle size and ζ-potential measurements were done in triplicate and averaged.

Synchrotron small angle X-ray scattering (SAXS)

SAXS measurements were carried out at the Austrian SAXS beamline at ELETTRA (Trieste, Italy). After pH adjustment, the OA and OA/LL-37 dispersions were sealed in thin-walled quartz capillaries. An X-ray beam with a wavelength of 1.54 Å (8 keV) was used, with a sample to detector distance of 1302 mm providing 0.07 < q < 5 nm^{-1}, where q is the length of the scattering vector, defined by $q = 4\pi/\lambda \sin(\theta/2)$, λ being the wavelength and θ being the scattering angle. 2D SAXS patterns were acquired for 20 s using a Pilatus 3 1M detector (Dectris Ltd, Baden, Switzerland; active area 169 × 179 mm^2 with a pixel size of 172 μm) and integrated into the one-dimensional (1-D) scattering function $I(q)$ using Fit2D and then analysed with IGOR pro (Wavemetrics Inc., Lake Oswego, OR). For each sample, six frames (20 s per frame) were recorded and averaged after

inspection for beam damage. No beam damage was observed in all investigated samples.

Additional SAXS measurements were performed on a Bruker Nanostar U (Bruker AXS, Karlsruhe, Germany) connected to a sealed-tube Cu anode X-ray source operating at 50 kV and 600 μA (Incoatec IμSCu, Geest-hacht, Germany). A Göbel mirror was used to convert the divergent polychromatic X-ray beam into a focused beam of mono-chromatic Cu K$_\alpha$ radiation (λ = 0.154 nm). The beam size was 0.3 mm. A sample to detector distance of 1075.5 mm gave the q-range 0.07 < q < 2.9 nm^{-1}. 2D SAXS patterns were acquired within 1 h using a VÅNTEC-2000 detector (Bruker AXS, Karlsruhe, Germany) with an active area of 140 × 140 mm^2 and a pixel size of 68 μm. Glassy carbon was measured with all samples for transmittance corrections, relative to the transmittance of the solvent.

The scattering curves are plotted as a function of relative intensity, I vs. q. Scattering from PBS was subtracted as a background from all samples before further analysis. A constant background was determined with a Porod extrapolation, $I(q) \propto q^{-4}$, and subtracted from the corresponding dataset. All measurements were done at room temperature.

The space groups of the liquid crystalline structures were identified by the relative position of their Bragg peaks in the scattering curves (see the ESI† for further information). Vesicles were identified by their characteristic q^{-2} dependence of $I(q)$ at low q values. Microemulsions were characterized by their broad correlation peak at intermediate q values, reflecting the mean droplet to droplet distance.

Results and discussion

Intermolecular interactions between LL-37 and OA in excess water control the colloidal structure and could play an important role in modulating the function of the designed peptide delivery system. The interaction of the AMP with the predominantly charged (at pH > pK_a of OA) and uncharged (at pH < pK_a of OA) lipid may further contribute to a fundamental understanding of the mechanism behind the AMP-driven destruction of the bacterial membrane. Therefore, it was important to understand the self-assembly of binary OA/LL-37 mixtures and the pH-triggered colloidal transformations in this system, with an attempt of introducing smart nanostructures for the delivery of the poorly water-soluble peptide LL-37.

LL-37 interaction with oleic acid at pH 7.0 and 7.5

The SAXS curves for OA emulsions prepared at pH 7.0 and 7.5 in Fig. 1 show a low-q upturn that is attributed to the scattering of large emulsion droplets with a defined volume. Additional Bragg reflections characteristic of an inverse $Fd3m$ type micellar cubic phase with a lattice constant of 14.4 nm inside the emulsion droplets were detected at pH = 7.0 (Fig. 1a). At pH = 7.5, the first three Bragg peaks of the inverse hexagonal (H$_2$) structure with a lattice constant of 6.1 nm in the interior of the emulsion droplets were observed (Fig. 1b).
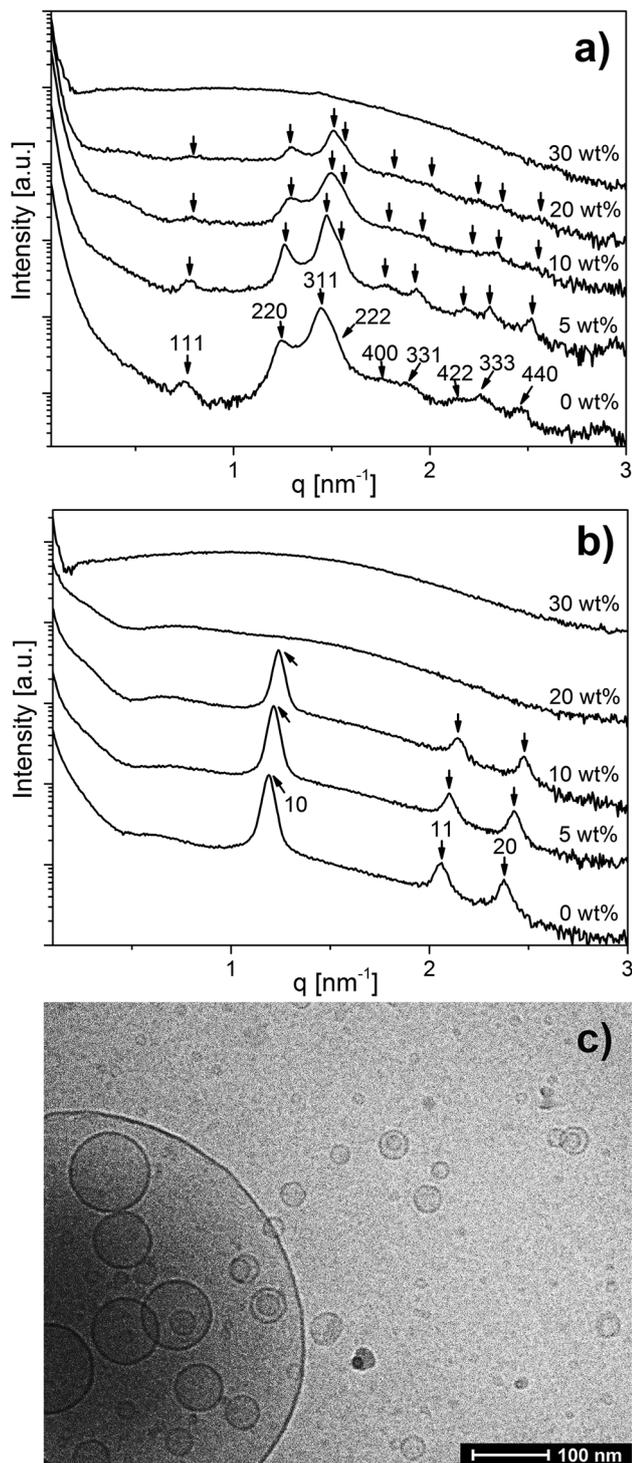
Fig. 1 Composition-dependent SAXS curves of emulsified OA and binary OA/LL-37 mixtures at LL-37 loading varying from 5–30 wt% in OA at (a) pH 7.0 and (b) pH 7.5. Emulsions were stabilized by F127. The identifiable Bragg peaks and further calculated theoretical peak positions are indexed with the corresponding Miller indices. (c) The cryo-TEM image of the OA/LL-37 dispersion containing 30 wt% LL-37 in OA that was prepared at pH 7.5.

These lattice dimensions are in good agreement with a previous report on normal OA emulsion.[11,43] In a concentration-dependent manner, the inclusion of LL-37 into OA emulsion droplets was associated with significant structural alterations at both pH values (see Fig. 1a and b). For the dispersions of the binary OA/LL-37 mixture containing 5–20 wt% LL-37 relative to OA at pH 7.0 (Fig. 1a), the Bragg reflections of the internal $Fd3m$ phase systematically shifted to larger q values with increasing LL-37 content, indicating a corresponding decrease in their lattice parameters from 14.4 to 13.8 nm (Fig. SI1a†). This shift in Bragg reflections was also observed for the internal H_2 structure at pH 7.5 upon integration of 5–10 wt% LL-37 in OA (Fig. 1b). The corresponding lattice constants of the H_2 phase decreased from 6.1 to 5.7 nm in this sample (see Fig. SI1b†).

A further increase in LL-37 content in OA above 20 wt% for the micellar cubosomes at pH = 7.0 (Fig. 1a) and 10 wt% for the hexosomes at pH = 7.5 (Fig. 1b) led to the disappearance of the Bragg reflections of both structures leading to more disordered phases. At 30 wt% LL-37 loading in OA at pH 7.0 and 20–30 wt% at pH 7.5, SAXS patterns characteristic of vesicles can be mostly seen, identified by their characteristic q^{-2} dependence of $I(q)$ at low q values. The corresponding cryo-TEM image of the same dispersion at pH 7.5, presented in Fig. 1c, also showed the presence of vesicular structures of various shapes and sizes. This was also confirmed by optical inspection of the samples, as the turbid OA/LL-37 dispersions at pH 7.0 and 7.5 started to lose their turbidity at a LL-37 content above 20 wt% and 10 wt% LL-37 in OA, respectively, due to the formation of relatively smaller self-assembled aggregates including vesicles and micelles (Fig. SI2 and SI3†).

In line with these results, DLS demonstrated a significant decrease in R_H from 190 nm (PDI = 0.244) to 105 nm (PDI = 0.349) when the LL-37 loading relative to OA increased from 20 wt% to 30 wt% at pH 7.0 (presented in Fig. SI2 and Table SI1†) and from 162 nm (PDI = 0.248) to 105 nm (PDI = 0.481) upon increasing the LL-37 concentration in OA from 10 wt% to 20 wt% at a pH of 7.5 (see Fig. SI3 and Table SI1†). The corresponding DLS correlation functions shown in Fig. SI3† exhibit only one decay, which is characteristic of a rather monomodal particle distribution. It seems then that the relatively large vesicles observed in Fig. 1c are only present in very small populations in the sample.

Hydrophobic and electrostatic interactions between OA and LL-37 molecules in excess PBS are thought to be responsible for the structural transformations upon modification in the composition of the emulsified binary OA/LL-37 system. The critical packing parameter (CPP) model with CPP = $v/(a_0 l)$ can be applied to predict the type of self-assembled structures based on the geometric considerations of the participating molecules.[50] In this model, v is the hydrophobic chain volume of the surfactant, a_0 is the effective headgroup area at the interface and l is the length of the hydrophobic tail of the molecule. At CPP values > 1 inverse, oil-continuous structures are expected, at CPP ~ 1 lamellar structures and at CPP < 1 direct, water-continuous structures.[50]

The detection of vesicles and normal micelles at relatively high concentrations of LL-37 in OA (above 20 wt% in OA at pH 7.0, and above 10 wt% in OA at pH 7.5) was in agreement with previous findings on the effect of LL-37 integration into the internal inverse *Im3m* type bicontinuous cubic structure of GMO-based cubosomes.[30] When comparing the GMO[30] and OA systems with the LL-37 content relative to OA below 20 wt% at pH 7.0 and 10 wt% at pH 7.5, within the *Fd3m* and H_2 regions of the emulsified OA system respectively, the loading of LL-37 resulted in a different structural response. The lattice constant of the nanostructure in the emulsified OA system decreases with increasing LL-37 content (an increase in the CPP). In the GMO system, loading LL-37 into cubosomes resulted in an increase in the lattice constant of the cubic structure (a decrease in CPP) up to almost 20 wt% LL-37 loading, followed by a transition to vesicles and micelles above 20 wt% LL-37 relative to GMO. Electrostatic interactions among the lipid and LL-37 molecules in excess PBS may be responsible for this different behavior. GMO is neutral and OA is negatively charged at a pH above its apparent pK_a. Hence, charge attraction among the cationic LL-37 molecules and the deprotonated, negatively charged OA headgroups at the OA–water interface could lead to a closer packing of the OA headgroups and a decrease in the effective headgroup area. This effect could result in an increase in the CPP in the emulsified OA system at pH 7.0 and 7.5 and would explain the observed shrinking of the nanostructures. However, at elevated LL-37 contents above 20 wt% in the OA system at pH = 7.5 and at 30 wt% at pH = 7.0, the higher density of LL-37 molecules at the OA interface may also lead to charge repulsion among the neighboring, positively charged LL-37 molecules. Together with steric effects, this may then result in an increase of the effective headgroup area of the lipid and induce structural transitions to phases with smaller CPP and hence more hydrophilic interfaces such as vesicles and micelles, in agreement with the results presented above. The reported hydrophobic and charge interactions of LL-37 with anionic OA may also contribute to a better understanding of the interactions of such AMPs with bacteria membrane lipids such as neutral and negatively charged phospholipids.[51–53] These intermolecular interactions are considered responsible for the attraction of AMPs to the bacterial cell membrane and may result in the transformation of the protective bilayer membrane into small vesicles and micelles at a relatively high AMP concentration in a detergent-like manner, as suggested by the results from this study.

The effect of pH on the emulsified OA/LL-37 system

Fig. 2 shows the effect of changing pH in the physiologically relevant range between 6.0 and 7.7 on the self-assembly of the control sample (OA emulsion) and OA/LL-37 dispersion containing 10 wt% LL-37 relative to OA. The SAXS curve of the normal (OA-in-water) emulsion at pH 6.0 showed a low-*q* upturn that was attributed to the scattering of relatively large emulsion droplets as discussed above. The absence of a significant correlation peak or any Bragg reflections indicates the absence of an internal nanostructure, similar to previous
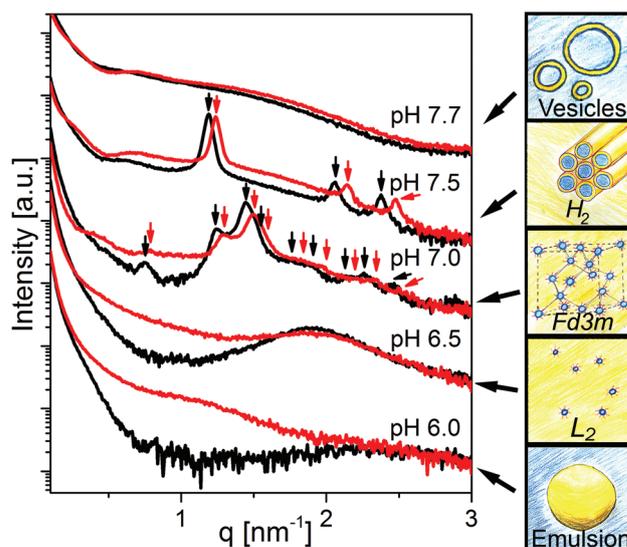

Fig. 2 pH-Dependent SAXS patterns of normal OA emulsions (black lines) and OA emulsions containing 10 wt% LL-37 loading relative to OA (red lines), both stabilized by F127. Transitions from normal emulsions to an emulsified L_2 phase, micellar cubosomes with an internal discontinuous cubic *Fd3m* phase, hexosomes with an internal H_2 phase, and vesicles were observed with increasing pH in the pH range of 6.0–7.7. Arrows index the identifiable and further calculated Bragg peaks of the cubic *Fd3m* and H_2 phases for samples at pH 7.0 and 7.5, respectively. The drawings represent an artistic view of the structural transitions in agreement with the SAXS patterns.

reports on the formation of large, structure-less oil droplets due to the self-assembly of triglycerides in water.[38] Upon increasing the pH to 6.5, a broad correlation peak at approximately $q = 1.9$ nm^{-1} appeared, indicating the formation of inverse micelles with a water core (L_2 phase) inside the emulsion droplets, referred to as emulsified microemulsions (EMEs). The effect of integrating LL-37 at 10 wt% relative to OA at the aforementioned pH values is also presented in Fig. 2. A substantial change in the structure was observed. At pH 6.0 and 6.5, a broad shoulder between $q \sim 0.5$ and 2.0 nm^{-1} appeared in the SAXS patterns of the investigated OA/LL-37 dispersions that were not detected in the pristine OA emulsion. This indicated the formation of relatively small nanoobjects coexisting with the OA emulsion droplets. The corresponding cryo-TEM of this sample at pH 6.5, presented in Fig. 3a, confirmed the results from SAXS: emulsified microemulsion droplets of around 100 nm in radius coexist with small particles of about 10 nm, most probably normal micelles. A small population of OA could be attracted to LL-37 through electrostatic or hydrophobic interactions, allowing self-assembly of smaller OA/LL-37 nanoparticles that coexist with the relatively bigger OA emulsion droplets. These smaller structures were not observed in pristine LL-37 in PBS, see the cryo-TEM image in Fig. SI4.†

When increasing the pH to 7.0, Bragg peaks from the inverse *Fd3m*-type micellar cubic structure appeared (Fig. 2). At pH 7.5, the observed Bragg reflections were from an inverse
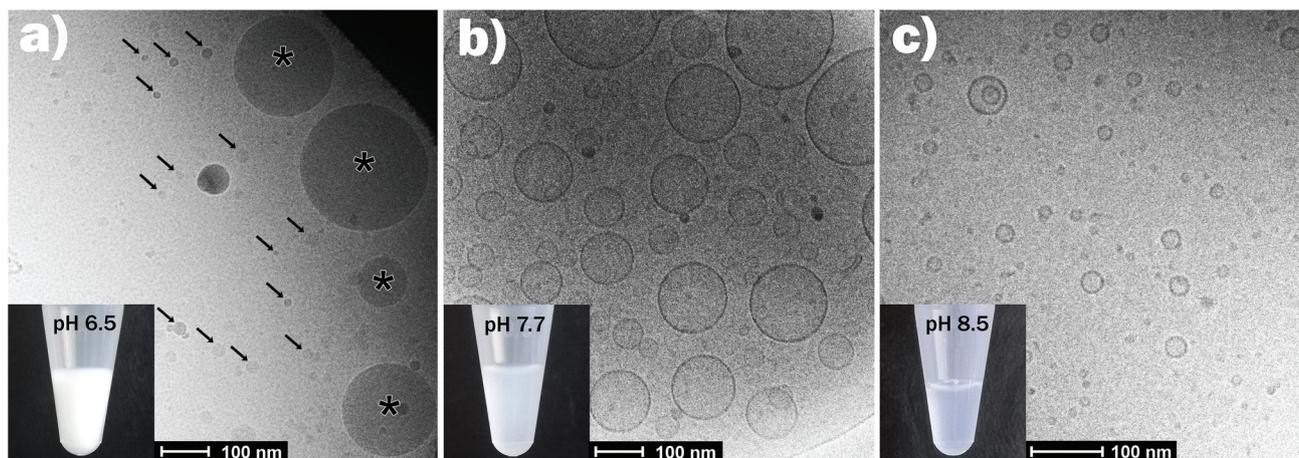
Fig. 3 Representative cryo-TEM images for the emulsions containing 10 wt% LL-37 relative to OA at pH = 6.5 (a), 7.7 (b), and 8.5 (c). The corresponding SAXS curves are presented in Fig. 2. In panel (a), the arrows point towards the smaller self-assemblies, coexisting with the larger EMEs (marked with asterisk). The pictures of the vials show that the dispersions became less turbid with increasing pH from 6.5 (mainly large EME droplets) to 8.5 (mainly small vesicles and micelles).

hexagonal (H_2) phase. In agreement with the discussion of the effect of LL-37 loading at constant pH 7.0 and 7.5 above, the lattice constants decreased in the presence of LL-37, as indicated by the shift in Bragg reflections to larger q-values. The characteristic reflections of the H_2 phase vanished at pH 7.7 in both systems, when scattering characteristics of vesicles were observed (q^{-2} upturn of $I(q)$ at low-q in both SAXS patterns). The cryo-TEM image of this sample with 10 wt% LL-37 in OA, as shown in Fig. 3b, confirms the presence of vesicles of various sizes and shapes, mostly above 50 nm in radius. A greater increase in pH to 8.5 led to a decrease in the vesicle size with greater potential for the formation of normal micelles. The majority of the small droplets in the cryo-TEM image of the sample at pH 8.5 (Fig. 3c) had a radius in the range of 5–10 nm. The colloidal transitions in this pH range as detected by SAXS and cryo-TEM were also consistent with the changes in the optical properties of the samples: the turbid emulsions at pH 6.5 became gradually less turbid upon transitioning to vesicles and micelles with increasing pH to 8.5.

In addition to SAXS and cryo-TEM, DLS confirmed the observed colloidal transformations for OA/LL-37 dispersion containing 10 wt% LL-37 in OA. The corresponding DLS correlation functions, as shown in Fig. 4, represent rather monomodal particles with a single relaxation time. Upon increasing the pH, the correlation functions shifted to shorter correlation times, signifying a decrease in the particle size (see Fig. 4a). The R_H of the particles, from the cumulative analysis of these correlation functions, decreased from 162 nm (PDI = 0.248) for the hexosomes at pH 7.5 to 124 nm (PDI = 0.439) for the vesicles at pH 7.7, and to 73 nm (PDI = 0.554) for the vesicles and micelles at pH 8.5 (see Table SI1†). The discrepancy between the value of R_H and the radius of the particles observed from the cryo-TEM images indicates the presence of some larger aggregates as they would give a much bigger contribution and

steer R_H to higher values even at small populations, as also evident from the polydispersity of this sample. This decrease in particle size with pH was consistent with the decrease in the light scattering intensity at pH > 7.5 (see Fig. 4c). This finding is in contrast to the previous DLS data on pristine OA dispersions that show an increase in the particle size with increasing pH in the range between 3 and 8 due to the formation of large vesicles.[11]

The SAXS curve for the system at 20 wt% LL-37 in OA at pH 5.4 presented in Fig. 5 shows the low-q upturn from large OA emulsion droplets. The $I(q)$ for this sample has a broad shoulder between $q \sim 0.5$ and 2.0 nm^{-1} potentially originating from the coexisting relatively small OA/LL-37 nanoparticles (see the discussion above). At pH 6.5, a broad correlation peak around $q \sim 1.9$ nm^{-1} appeared in the scattering, indicating the formation of EMEs. The SAXS curves between pH = 6.7 and 7.4 showed the Bragg reflections of the cubic $Fd3m$ phase that gradually shifted to smaller q values with increasing pH. The corresponding lattice constants of the $Fd3m$ phase were 12.5 and 16.5 nm at pH 6.7 and 7.4, respectively. At pH 7.5, a scattering profile characteristic of vesicles was observed. The structural transitions from hierarchically organized droplets with an internal $Fd3m$ structure to simple vesicles upon increasing pH appeared reversible upon changing the pH between 5.4 and 7.5 (see the color coded SAXS patterns in Fig. 5).
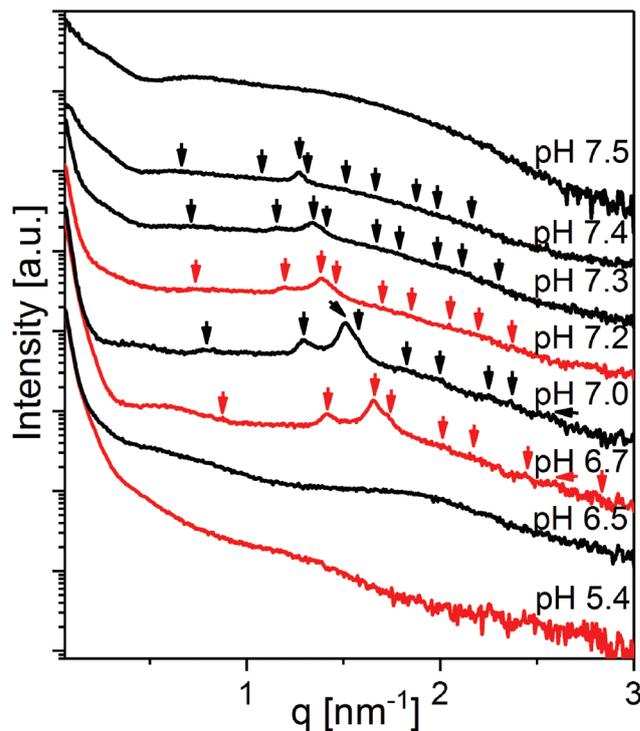
To further investigate the effect of increasing LL-37 concentration, the LL-37 loading was increased to 30 wt% relative to OA (see Fig. 6). At such a high LL-37 loading, the SAXS profile at pH 5.9 and 6.5 showed a low-q upturn from large droplets with a diffuse local maximum at $q \sim 0.6$ nm^{-1} and a shoulder around $q \sim 1.5$ nm^{-1}, more pronounced at pH 6.5. This indicates the coexistence of relatively small OA/LL-37 nanoparticles with the large, but mostly unstructured emulsion droplets, as reported above for the emulsified systems containing a lower content of LL-37 around this pH value. At pH 6.9, two Bragg
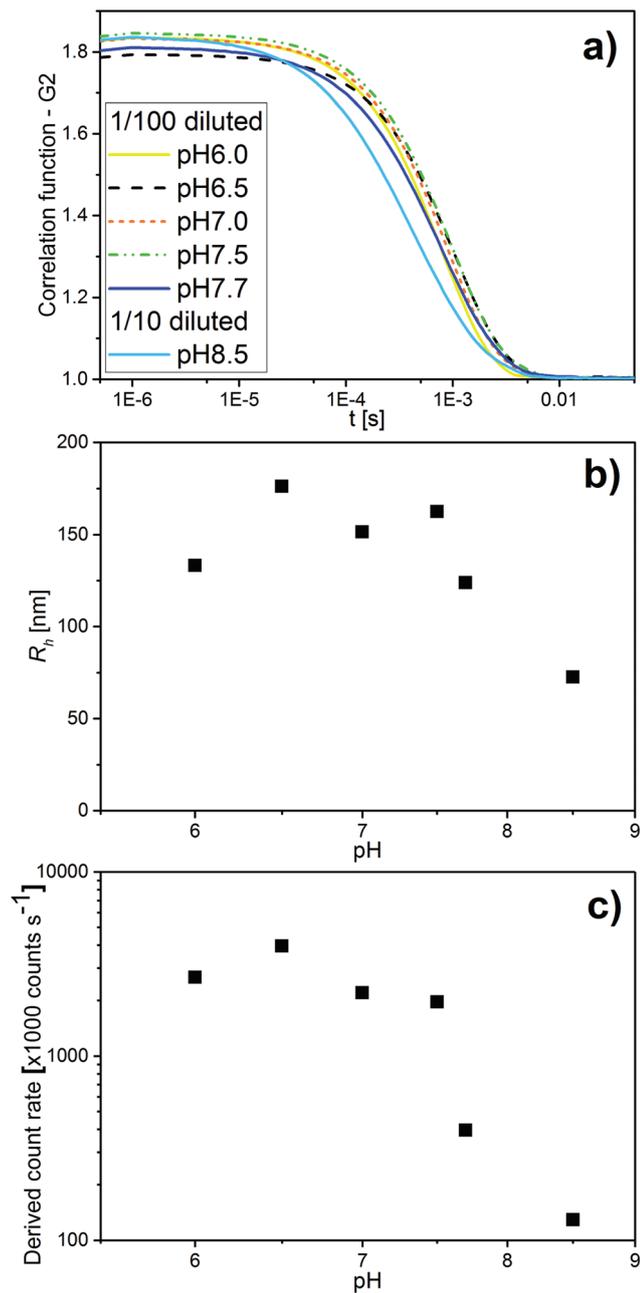
Fig. 4 (a) pH-Dependent DLS correlation functions for emulsions containing 10 wt% LL-37 in OA at different pH values in the range of 6.0−8.5. (b) The corresponding R_H values determined with the cumulative analysis from the correlation functions in (a) (see also Table SI2† for the corresponding R_H and PDI values). (c) The corresponding light scattering intensity in this pH range.

Fig. 5 pH-Dependent SAXS curves of the OA emulsions with 20 wt% LL-37 loading, stabilized by F127. The black curves were taken from dispersions measured with increasing pH from 6.5 to 7.5 and the red curves from the same dispersions when the pH was decreased from 7.5 to 5.4. The identifiable Bragg peaks and further calculated theoretical peak positions of the discontinuous cubic $Fd3m$ structure are indexed with arrows.

reflections, potentially corresponding to the micellar cubic $Fd3m$ phase, were identified in the scattering pattern.

Between pH 7.0 and 7.5, the two proposed $Fd3m$ Bragg reflections diminished and the $I(q)$ patterns indicate that vesicles and micelles are the dominating structures up to pH = 8.5, the highest pH value investigated in this study. Complementary cryo-TEM experiments on this system at pH =

8.5 (see Fig. 6b and Fig. SI5†) indicate the presence of elongated thread like nano-objects such as elongated vesicles or bilayer fragments, some reaching over 100 nm in length, coexisting with relatively small spherical vesicles of around 10–20 nm in radius.

The pH-dependent DLS measurements of this sample also demonstrated a decrease in R_H from about 155 nm (PDI = 0.324) for the large emulsion droplets at pH 6.5 to about 105 nm (PDI = 0.349) for the dominating vesicles at pH 7.0, and about 57 nm (PDI = 0.509) for the small vesicles at pH 7.7 (see Fig. SI6 and Table SI2†). Increasing the pH to 8.5 resulted in a further decrease in particle size, reducing the intensity of the light scattered from the particles by a factor of 3.2 so that the collected data were not sufficient for a cumulative analysis. An additional measurement of the same sample with a 1/10 instead of 1/100 dilution at pH 8.5 estimated R_H to be 31 nm (PDI = 0.468).

ζ-Potential measurements were performed to link the pH-induced colloidal transformations to the modified surface charge of the OA/LL-37 nano-objects. These measurements were carried out at different pH values and showed a decrease in the charge of the nanoparticles from around −2 to −40 mV in the OA nano-self-assemblies upon increasing the pH from 6.0 to 9.0 (see Fig. SI7†). The sigmoidal shape of these curves
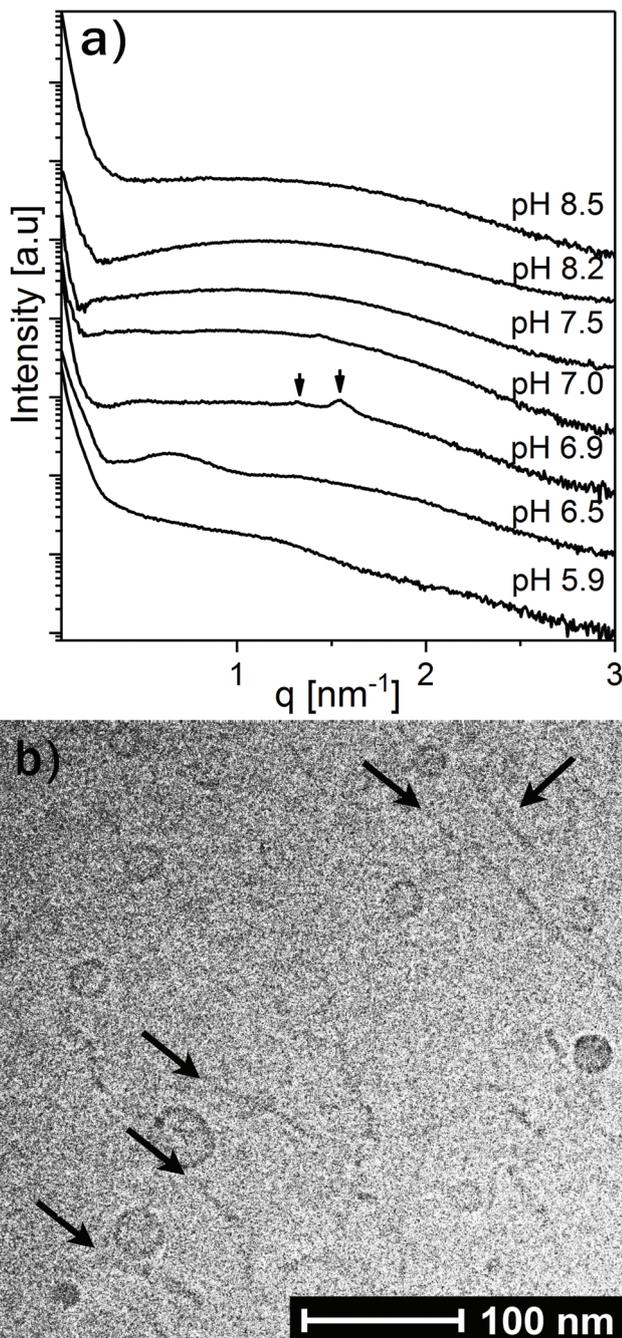
Fig. 6 (a) SAXS patterns at increasing pH for OA emulsions loaded with 30 wt% LL-37 and stabilized by F127. Identifiable Bragg reflections from a potential micellar cubic $Fd3m$ phase at pH 6.9 are marked with arrows. (b) Representative cryo-TEM image of the corresponding dispersion at pH 8.5. Thin thread-like cylindrical micelles and/or bilayer fragments (marked with arrows) coexisting with small vesicles were observed.

allowed the estimation of the apparent pK_a of OA in the self-assembled structures from their point of inflection. The resulting apparent pK_a of OA in the investigated OA/LL-37 dispersions containing LL-37 between 0 and 20 wt% in the binary OA/LL-37 mixture was around 7.8, in agreement with the occurrence of the major colloidal transformations around this

pH reported from the SAXS analysis above. However, the slope of the ζ-potential *vs.* pH curves decreased with increasing LL-37 content in OA and the sigmoidal trend diminished at ~30 wt% LL-37 in OA. This indicates that the interaction between LL-37 and OA favors the deprotonation of OA even at lower pH values. This decrease in ζ-potential with pH further confirmed the protonation behavior of OA as the driving force for the detected pH-triggered structural transformations in these OA/LL-37 self-assemblies.

The successive deprotonation with increasing pH and the resulting charge repulsions among the negatively charged carboxylic headgroups of OA molecules led to an increase in the effective headgroup area of OA at the OA–water interface inducing a decrease in the CPP. It was associated with significant structural changes. This is in agreement with the observed phase transitions to more hydrophilic structures such as vesicles or micelles at pH values close to or above the estimated apparent pK_a of OA in the presence and absence of LL-37. Contrary to its CPP-increasing effect at constant pH of 7.0 and 7.5 and at loadings below 20 wt% LL-37 in OA as reported above, the integration of LL-37 into the OA–water interface at pH values greater than the apparent pK_a decreased the CPP. This explains the tendency of OA/LL-37 mixtures to form vesicles and micelles in excess PBS. For instance, the presence of 10 wt% LL-37 relative to OA favored the formation of small vesicles and normal micelles at pH 8.5, whereas only large uni- and multi-lamellar vesicles were previously reported in the OA system at a pH around 8.5.[11,36] The phase transitions from hierarchically organized emulsions to vesicles and micelles occurred at even lower pH = 7.0 when increasing the LL-37 loading to 30 wt% relative to OA. The self-assembly of pristine OA into cylindrical micelles has also been previously reported at pH values above 10.[33,36] The appearance of such structures at a lower pH = 8.5 in the OA sample with 30 wt% LL-37 loading further confirmed the decreasing effect of LL-37 on the CPP in this pH range.

Fig. 7 summarizes the experimental findings of the present work in the form of a phase diagram. This diagram represents the detectable structures occurring in the dispersed OA/LL-37 self-assemblies in different pH regimes and LL-37 concentrations in the binary OA/LL-37 mixtures in the range of 0–30 wt%. Each point on the diagram represents the detected structures based on a SAXS experiment or a cryo-TEM observation and the colored phase boundaries are drawn for visual guidance only. It should be noted that in cases where coexisting phases are present, the structure with the higher SAXS scattering intensity (the intensity of Bragg peaks) was selected. The phase diagram suggests two major trends in this system: more hydrophilic structures are favored when (i) the pH is increased and (ii) the LL-37 content is above a specific threshold concentration that decreases with increasing pH (*i.e.* 30 wt% and 20 wt% LL-37 in OA at pH 7.0 and 7.5, respectively).

The transition from highly ordered inverse structures such as discontinuous $Fd3m$ and H_2 phases to flattened bilayers (vesicles) in the emulsified OA/LL37 system is interesting in
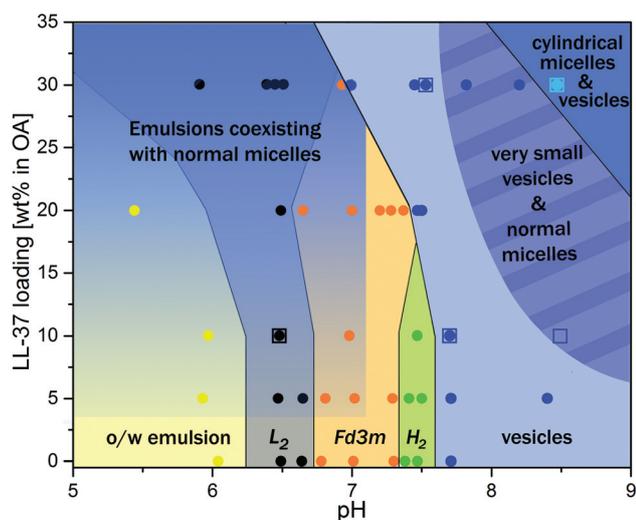
Fig. 7 Phase behavior of OA/LL-37 dispersions that were stabilized by F127. The pH-composition phase diagram was constructed by using SAXS experiments and cryo-TEM observations. Each point on the graph represents a separate SAXS (circles) or a cryo-TEM (opened squares) measurement. The lines between phases are for visual guidance and do not indicate sharp phase boundaries. The gradient in the emulsion regions indicates their coexistence with an increasing content of OA/LL-37 micelles. In other coexistence regions, only the phase dominating the SAXS signal is shown.

the design of pH-responsive antimicrobial nanosystems. In a recent study on the antimicrobial activity of GMO/LL-37 nano-self-assemblies, it was found that the antimicrobial activity is directly correlated with the nanostructural features of the nanoparticles.[30,31] The challenge for the rational design of novel therapeutic self-assembled nanocarriers is in unraveling the relationship between the composition, the nanostructural properties and the biological activity. Therefore, further studies focusing on the biological activity of these OA/LL-37 nano-self-assemblies are still needed. In these studies, one should bear in mind that the nanostructure–activity correlation depends on different factors including the pH and bacteria strain. The detailed insights into the interactions between OA and LL-37 from this work may provide a framework for the future design of pH-responsive antimicrobial nanobiointerfaces for passive targeting of bacterial infected tissues in the body.

Summary and conclusions

pH-Tunable nanocarriers for the delivery of poorly water soluble AMPs such as LL-37 were prepared through self-assembly of the peptide with OA in excess water. The resulting OA/LL-37 self-assemblies showed a strong response to variations in the composition and pH. LL-37 could be integrated up to ~20 wt% relative to OA into the OA based micellar cubosomes at pH 7.0, and up to ~10 wt% into the respective hexosomes at pH 7.5. A further increase in the LL-37 content led to the trans-

formation of these highly ordered structures into more disordered vesicles and normal micelles. In normal OA emulsions at pH 6.0, increasing the LL-37 content from 0–30 wt% relative to OA led to the gradual formation of micelles coexisting with the larger emulsion droplets. The OA/LL-37 self-assemblies were shown to be highly pH-responsive within the physiological pH between 5.0 and 8.5: a pool of colloidal structures and transformations were observed ranging from normal, mostly unstructured emulsions to emulsified microemulsions, highly ordered micellar cubosomes and hexosomes, and vesicles coexisting with micelles upon increasing the pH. The results suggest that hydrophobic and electrostatic interactions among OA and LL-37 molecules are driving the detected structural transformations with both composition and pH.

Understanding the influence of pH and composition on the nanostructural transformations of self-assembled soft systems containing pH-responsive lipid molecules is important to control and trigger the self-assembly in these systems. The structural changes presented in this study are interesting for the further development of pH-driven nanocarriers for the targeted delivery of poorly water-soluble AMPs as an alternative to conventional antibiotics. They may also be valuable for a further understanding of the mechanism behind the AMP-induced disruption of the bacterial cell membrane.

Conflicts of interest

There are no conflicts to declare.

Acknowledgements

References

1   S. Salentinig, K. J. Tangso, A. Hawley and B. J. Boyd, *Langmuir*, 2014, **30**, 14776.
2   R. Negrini and R. Mezzenga, *Langmuir*, 2011, **27**, 5296.
3   G. Zhu, J. N. Mock, I. Aljuffali, B. S. Cummings and R. D. Arnold, *J. Pharm. Sci.*, 2011, **100**, 3146.
4   C. C. Pak, S. Ali, A. S. Janoff and P. Meers, *Biochim. Biophys. Acta*, 1998, **1372**, 13.
5   F. S. Poletto, F. S. Lima, D. Lundberg, T. Nylander and W. Loh, *Colloids Surf., B*, 2016, **147**, 210.
6   C. Yao, P. Wang, X. Li, X. Hu, J. Hou, L. Wang and F. Zhang, *Adv. Mater.*, 2016, **28**, 9341.

7 M. A. Azagarsamy, D. L. Alge, S. J. Radhakrishnan, M. W. Tibbitt and K. S. Anseth, *Biomacromolecules*, 2012, **13**, 2219.

8 W. K. Fong, T. L. Hanley, B. Thierry, A. Hawley, B. J. Boyd and C. B. Landersdorfer, *J. Controlled Release*, 2016, **228**, 67.

9 X. Q. Wang and Q. Zhang, *Eur. J. Pharm. Biopharm.*, 2012, **82**, 219.

10 R. Negrini, W. K. Fong, B. J. Boyd and R. Mezzenga, *Chem. Commun.*, 2015, **51**, 6671.

11 S. Salentinig, L. Sagalowicz and O. Glatter, *Langmuir*, 2010, **26**, 11670.

12 W. Gao, J. M. Chan and O. C. Farokhzad, *Mol. Pharm.*, 2010, **7**, 1913.

13 R. E. Hancock and H. G. Sahl, *Nat. Biotechnol.*, 2006, **24**, 1551.

14 G. S. Wang, in *Antimicrobial Peptides: Discovery, Design and Novel Therapeutic Strategies*, ed. G. S. Wang, CABI, Oxfordshire UK, 2nd edn, 2017, ch. 1, p. 1.

15 Y. Kai-Larsen and B. Agerberth, *Front. Biosci.*, 2008, **13**, 3760.

16 U. H. N. Dürr, U. S. Sudheendra and A. Ramamoorthy, *Biochim. Biophys. Acta*, 2006, **1758**, 1408.

17 X. Zhang, K. Oglecka, S. Sandgren, M. Belting, E. K. Esbjorner, B. Norden and A. Graslund, *Biochim. Biophys. Acta*, 2010, **1798**, 2201.

18 D. Xhindoli, S. Pacor, M. Benincasa, M. Scocchi, R. Gennaro and A. Tossi, *Biochim. Biophys. Acta*, 2016, **1858**, 546.

19 M.-D. Seo, H.-S. Won, J.-H. Kim, T. Mishig-Ochir and B.-J. Lee, *Molecules*, 2012, **17**, 12276.

20 L. de Campo, A. Yaghmur, L. Sagalowicz, M. E. Leser, H. Watzke and O. Glatter, *Langmuir*, 2004, **20**, 5254.

21 S. T. Hyde, *Curr. Opin. Solid State Mater. Sci.*, 1996, **1**, 653.

22 J. M. Seddon, *Biochim. Biophys. Acta*, 1990, **1031**, 1.

23 P. Mariani, V. Luzzati and H. Delacroix, *J. Mol. Biol.*, 1988, **204**, 165.

24 V. Luzzati and F. Husson, *J. Cell Biol.*, 1962, **12**, 207.

25 J. Barauskas, M. Johnsson and F. Tiberg, *Nano Lett.*, 2005, **5**, 1615.

26 L. Sagalowicz, M. E. Leser, H. J. Watzke and M. Michel, *Trends Food Sci. Technol.*, 2006, **17**, 204.

27 L. Boge, A. Umerska, N. Matougui, H. Bysell, L. Ringstad, M. Davoudi, J. Eriksson, K. Edwards and M. Andersson, *Int. J. Pharm.*, 2017, **526**, 400.

28 T. G. Meikle, A. Zabara, L. J. Waddington, F. Separovic, C. J. Drummond and C. E. Conn, *Colloids Surf., B*, 2017, **152**, 143.

29 A. Chemelli, M. Maurer, R. Geier and O. Glatter, *Langmuir*, 2012, **28**, 16788.

30 M. Gontsarik, M. T. Buhmann, A. Yaghmur, Q. Ren, K. Maniura-Weber and S. Salentinig, *J. Phys. Chem. Lett.*, 2016, **7**, 3482.

31 L. Boge, H. Bysell, L. Ringstad, D. Wennman, A. Umerska, V. Cassisa, J. Eriksson, M.-L. Joly-Guillou, K. Edwards and M. Andersson, *Langmuir*, 2016, **32**, 4217.

32 G. Cevc, J. M. Seddon, R. Hartung and W. Eggert, *Biochim. Biophys. Acta, Biomembr.*, 1988, **940**, 219.

33 K. Edwards, M. Silvander and G. Karlsson, *Langmuir*, 1995, **11**, 2429.

34 D. P. Cistola, D. Atkinson, J. A. Hamilton and D. M. Small, *Biochemistry*, 1986, **25**, 2804.

35 D. P. Cistola, J. A. Hamilton, D. Jackson and D. M. Small, *Biochemistry*, 1988, **27**, 1881.

36 K. Suga, D. Kondo, Y. Otsuka, Y. Okamoto and H. Umakoshi, *Langmuir*, 2016, **32**, 7606.

37 S. Salentinig, S. Phan, T. A. Darwish, N. Kirby, B. J. Boyd and E. P. Gilbert, *Langmuir*, 2014, **30**, 7296.

38 S. Salentinig, L. Sagalowicz, M. E. Leser, C. Tedeschi and O. Glatter, *Soft Matter*, 2011, **7**, 650.

39 S. Salentinig, S. Phan, J. Khan, A. Hawley and B. J. Boyd, *ACS Nano*, 2013, **7**, 10904.

40 S. Salentinig, S. Phan, A. Hawley and B. J. Boyd, *Angew. Chem., Int. Ed.*, 2015, **54**, 1600.

41 S. Salentinig, H. Amenitsch and A. Yaghmur, *ACS Omega*, 2017, **2**, 1441.

42 J. D. Kaspersen, J. N. Pedersen, J. G. Hansted, S. B. Nielsen, S. Sakthivel, K. Wilhelm, E. L. Nemashkalova, S. E. Permyakov, E. A. Permyakov, C. L. Pinto Oliveira, L. A. Morozova-Roche, D. E. Otzen and J. S. Pedersen, *ChemBioChem*, 2014, **15**, 2693.

43 M. Nakano, T. Teshigawara, A. Sugita, W. Leesajakul, A. Taniguchi, T. Kamo, H. Matsuoka and T. Handa, *Langmuir*, 2002, **18**, 9283.

44 J. Borne, T. Nylander and A. Khan, *J. Colloid Interface Sci.*, 2003, **257**, 310.

45 S. P. Barros, R. Williams, S. Offenbacher and T. Morelli, *Periodontol. 2000*, 2016, **70**, 53.

46 M. Bickel and G. Cimasoni, *J. Periodontal Res.*, 1985, **20**, 35.

47 I. Kleinberg and G. Hall, *J. Periodontal Res.*, 1969, **4**, 109.

48 H. H. Leveen, G. Falk, B. Borek, C. Diaz, Y. Lynfield, B. J. Wynkoop, G. A. Mabunda, J. L. Rubricius and G. C. Christoudias, *Ann. Surg.*, 1973, **178**, 745.

49 L. A. Schneider, A. Korber, S. Grabbe and J. Dissemond, *Arch. Dermatol. Res.*, 2007, **298**, 413.

50 J. N. Israelachvili, D. J. Mitchell and B. W. Ninham, *J. Chem. Soc., Faraday Trans. 2*, 1976, **72**, 1525.

51 D. J. Paterson, M. Tassieri, J. Reboud, R. Wilson and J. M. Cooper, *Proc. Natl. Acad. Sci. U. S. A.*, 2017, **114**, E8324.

52 A. A. Strömstedt, L. Ringstad, A. Schmidtchen and M. Malmsten, *Curr. Opin. Colloid Interface Sci.*, 2010, **15**, 467.

53 Y. Shai, *Pept. Sci.*, 2002, **66**, 236.